Characterization of shallow high-amplitude seismic anomalies in the Hoop Fault Complex, Barents Sea

Satinder Chopra[1], Ritesh Kumar Sharma[1], Graziella Kirtland Grech[1], and Bent Erlend Kjølhamar[2]

Abstract

The shallow migrating hydrocarbon fluids in the western Barents Sea are usually found to be associated with high seismic amplitudes. We have attempted to characterize such shallow high-amplitude anomalies in the Hoop Fault Complex area of the western Barents Sea. The workflow is devised for discrimination of anomalies that are associated with the presence of hydrocarbons from those that are not, and quantifying them further includes the computation of a set of seismic attributes and their analyses. These attributes comprise coherence, spectral decomposition, prestack simultaneous impedance inversion, and extended elastic impedance attributes, followed by their analysis in an appropriate crossplot space, as well as with the use of rock-physics templates. Finally, we briefly evaluate the futuristic efforts being devoted toward the integration of diverse data types such as P-cable seismic as well as controlled-source electromagnetic data so as to come up with an integrated assessment for the prospects and to mitigate risk.

Introduction

Many areas of the western Barents Sea host shallow as well as deep-seated hydrocarbon accumulations, wherefrom fluids are migrating to the seafloor (Bünz et al., 2012, 2014; Bünz and Chand, 2013). Evidence of past episodes of gas migration can be seen in the form of pockmarks on the seafloor as well as vertical pipes or chimneys on seismic sections (Plaza-Faverola et al., 2011). Natural gas hydrates are also present in some areas (Chand et al., 2012), and free gas is present below the base of the hydrate stability layer that is typically shallow. Such shallow migrating hydrocarbon fluids as well as free gas below the hydrates represent potential hazards for drilling deeper wells and the construction of seabed installations. Thus, the detailed distribution of shallow migrating fluids or the presence of gas in the shallow zones in the areas under investigation is required, for which data with high vertical and spatial resolution are required.

We begin by explaining succinctly the geologic setting of the western Barents Sea and in particular the Hoop Fault Complex (HFC) area we focus on. This is followed by our observations of high-amplitude anomalies on the shallow sections of the seismic data, whose characterization is our objective. With the water bottom starting at close to 600 ms or so, the term "shallow" refers roughly to the top one second of seismic data. Thereafter, we discuss and present the results of a workflow that was adopted for the discrimination of some of the high-ampli-

tude anomalies. This workflow entails the application of coherence, spectral decomposition, poststack impedance inversion, going on to prestack simultaneous impedance inversion and extended elastic impedance (EEI), followed by the analysis of the results in different crossplot spaces, using rock-physics templates (RPTs). The quantitative interpretation workflow followed has helped us high-grade amplitude anomalies that are associated with hydrocarbons with a high level of confidence.

Finally, we briefly discuss the efforts being made in our industry for integration of seismic data with other types of data that are being acquired with state-of-the-art technology, all being aimed at mitigating exploration risk.

Geologic setting
Location

The Barents Sea forms part of the Arctic Ocean that is a continental shelf surrounded by islands, archipelagos, and peninsulas (Figure 1). It is bordered by the Svalbard and Franz Josef Land archipelagos to the north, the shelf edge toward the Norwegian-Greenland Sea, Novaya Zemlya to the east, and the Norwegian Coast and Kola Peninsula to the south.

Basin evolution

The western part of the Barents Sea (indicated with the pink dashed square in Figure 1) can be divided into

---

[1]Arcis Seismic Solutions, Calgary, Canada and TGS, Asker, Norway. E-mail: Satinder.Chopra@tgs.com; Ritesh.Sharma@tgs.com; Graziella.KirtlandGrech@tgs.com.

[2]TGS, Asker, Norway. E-mail: benterlend.kjolhamar@tgs.com.

three geologic components, namely, the Svalbard Platform; the area between the Svalbard Platform and the Norwegian Coast; and the western continental margin, which developed close to and along a mega shear system (De Geer Zone) that linked the rifting and spreading in the Norwegian-Greenland Sea to the Eurasian Basin (Faleide et al., 2008).

The key elements making up a structural play are usually referred to as its structural elements, e.g., the tectonic context of the whole structural evolution, the subsurface deformation that results in the formation of traps, reservoirs and seals, and the overall 3D geometry of the structural play. The western Barents Sea exhibits a complex tectonic interplay between the western and northwestern margins of the Eurasian plate resulting in the development of basins, platforms, structural highs, and fault complexes. Over these structural elements in the western Barents Sea, a clear dominance of the east–northeast/west–southwest fault (HFC and others) imprints stand out, which resulted due to the tectonic evolution of the area. Different tectonic phases, namely, the Late Devonian-early Carboniferous (Figure 2), the Permian rifting (Faleide et al., 1984; Glørstad-Clark et al., 2010), and the middle Jurassic-early Cretaceous and Cenozoic phases, have influenced the structural elements.
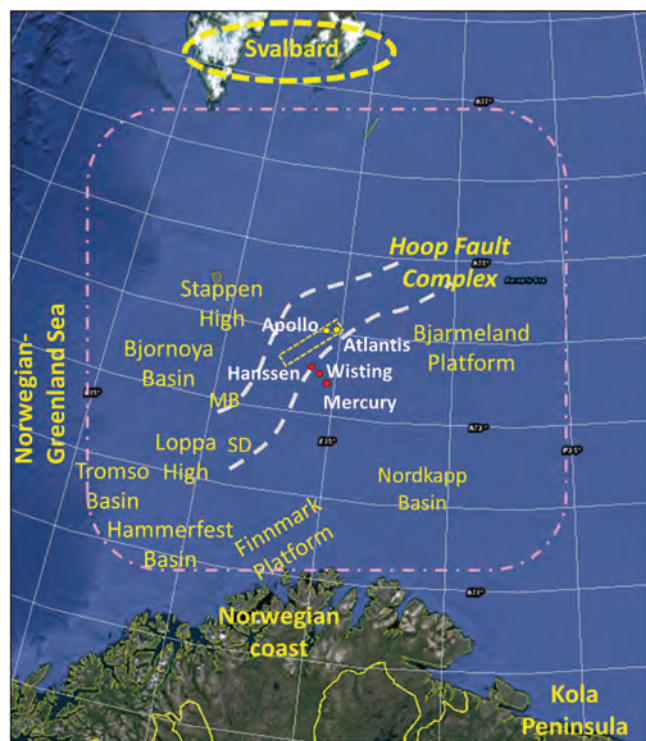
Figure 1. Location map showing the western Barents Sea and some of the structural elements in that area. The corridor in white thick dashed lines shows the Hoop Fault system running roughly in a northeast–southwest direction. The location of the seismic data volume that was picked up for the present study is shown with the yellow dashed rectangle, and falls within the Hoop Fault corridor. The drilled wells are marked in white. SD: Svalis Dome; MB: Maud Basin (image generated using Google Earth).

The Paleozoic and Mesozoic evolution of western Barents Sea experienced several tectonic events, including rifting, faulting, and uplifting, interspersed with regional subsidence and sedimentation. Thus, block faulting in shale, claystone, siltstone, limestone, and dolomite lithounits is seen in this area.

HFC system

With the changing tectonic stress fields in the area, some of the earlier fault trends also got reactivated, leading to complex fault systems. The HFC system is one such system that cuts across the Loppa High and Bjarmeland Platform. It is characterized by normal block faulting that exhibits a swarm of normal faults cutting the Bjarmeland Platform (Figure 1). The central part of the fault system may have controlled the Late Carboniferous to Permian sedimentation and development of the Maud Basin and Svalis Dome. To the south, the HFC comprises a narrow graben that forms a part of the en echelon fault patterns in northern Loppa High (Gabrielsen et al., 1990). In short, all these geologic discontinuity features are prevalent in and around the ribbon shown as dashed white lines in Figure 1.

In Figure 3, we show a south–north seismic section in the Hoop Fault area, and the faults are seen cutting the Carboniferous and the older strata (green and white arrows) as well as the Permian, Triassic, Jurassic, Cretaceous, and younger strata. All these faults comprise the Hoop Fault System. The Hoop Fault Graben that formed as a result of faulting is also seen in the middle.

Brief exploration history

Encouraged by the success of hydrocarbon exploration in the North Sea in the 1960s, the Norwegian authorities opened up the western Barents Sea to determine the
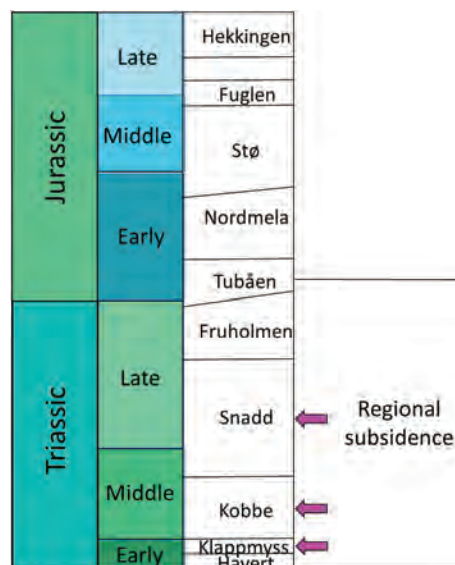
Figure 2. Generalized stratigraphy of the western Barents Sea around the zone of interest (modified from Glørstad-Clark et al., 2010).

hydrocarbon potential in the area. Beginning with some gas discoveries in 1980s, including the famous Snøhvit gas field in 1984 (being the first offshore development in the Barents Sea that came on-stream in 2007), and the Goliat oil field discovered in 2000, and started production in March 2016.

The HFC is one of the core areas in the Norwegian 23rd licensing round, and has been the focus area for several exploration companies since 2009.

The Wisting Central well 7324/8-1 drilled in 2013 and the Hanssen well 7324/7-2 drilled in 2014 proved light oil in Jurassic fault blocks 500–800 m below the seabed. Although the Apollo well 7324/2-1 drilled (to a depth of 1050 m or so reaching just below the Stø Formation) in June 2014 came out dry, the Atlantis well 7325/1-1 drilled (to a depth of 2800 m penetrated well below the Kobbe Formation) in July 2014, and the Mercury well 7324/9-1 drilled in August 2015, resulted in small gas discoveries.

Prospective reservoir rocks in HFC

As mentioned above, post-Eocene erosion removed much of Cretaceous and some younger strata in the HFC area, making the older strata open for exploration. In some areas of the HFC, the Carboniferous and Permian units are shallow enough to be considered as exploration targets. Carbonate rocks that experienced erosion and developed good porosity are also possible targets.

The deltaic deposits of the Triassic can be seen on the seismic data as large-scale northwest-prograding clinoform packages thinning in that direction. The sandstone channels in the Klappmyss, Kobbe, and Snadd Formations (purple arrows in Figure 2) are prospective in the HFC. Figure 4 shows a segment of a seismic section CC′. Beside the bright amplitude anomalies that stand out on the section, the clinoform signatures are also clearly seen.

The Atlantis well 7325/1-1 tested the Triassic section in a large closure adjacent to the Hoop Graben. Although the main target was the Middle Triassic Kobbe Formation, the well made a small discovery in the Upper Triassic sands. Shallow stratigraphic boreholes drilled near the Svalis Dome have confirmed the Middle Triassic Steinkobbe Member of the Kobbe Formation as an excellent quality oil-prone marine source rock. As well, large deltaic channel systems of the Upper Triassic Snadd Formation can be seen as bright amplitude anomalies on the seismic data.

Based on the exploration work carried out so far, the Jurassic succession in the HFC area has been the most successful. The Upper Jurassic Hekkingen Formation (Figure 2) source rock is believed to be mature along the western and southern flanks of the basins adjacent to the HFC. The two recent wells, Wisting Central and Hanssen proved oil in the Jurassic fault blocks between 500 and 800 m below the seafloor. Both these discoveries were supported by bright amplitude anomalies on the seismic.

Availability of seismic data and workflow adopted

A portion (500 km^2) of the 3D seismic volume covering more than 22,000 km^2 in and around the HFC was picked up for carrying out a feasibility analysis aimed at characterizing the bright seismic amplitude anomalies, and also examining the fault and channel features in
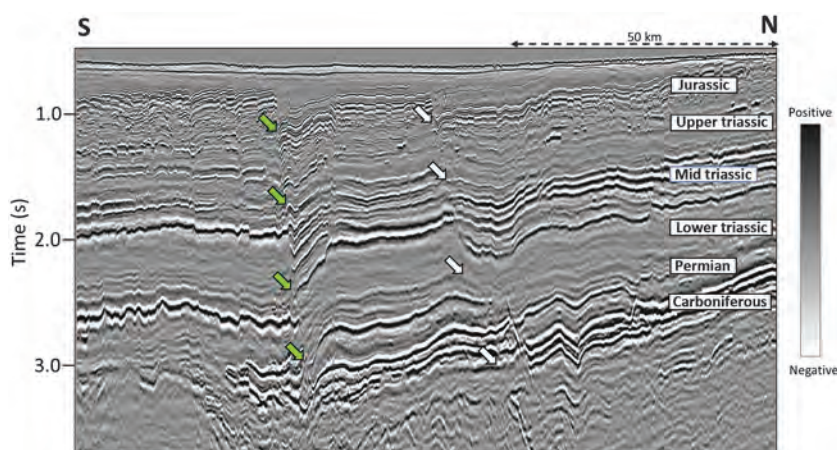
Figure 3. A representative south–north seismic section in the Hoop Fault area. The area has a condensed geologic succession visible here from a Devonian or older seismic basement to the Lower Cretaceous with a thin Quaternary cover. The main reservoir-prone units are Permian karstified carbonates, Mid-Triassic and Upper Triassic sandstones, Lower to Mid-Jurassic sandstones, and potentially Barremian sandstones. The main source rocks are of Mid-Triassic and Upper Jurassic age.
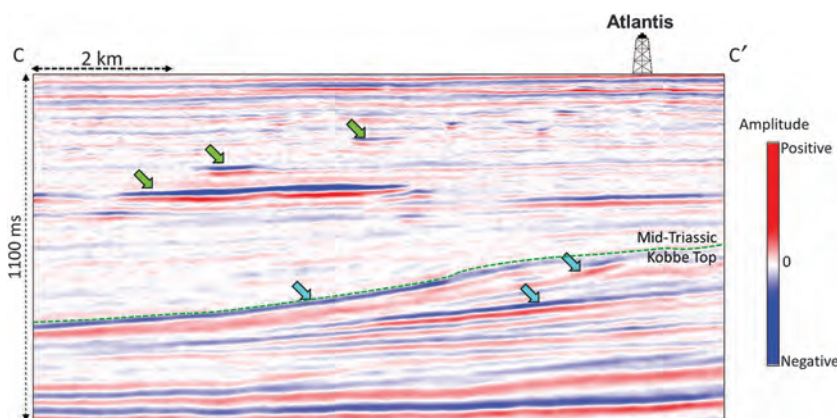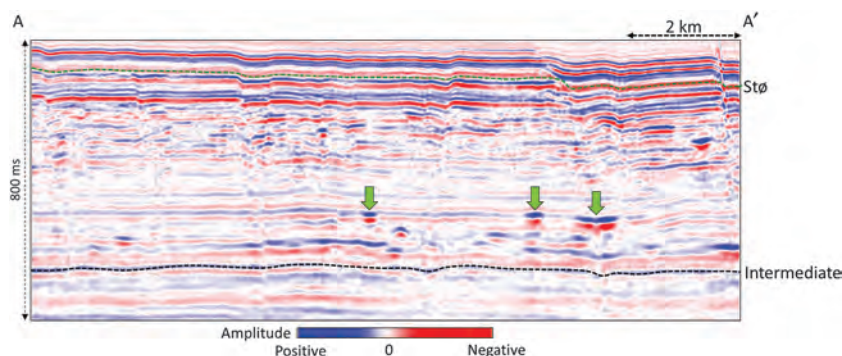

Figure 4. Crossline CC′ passing through Atlantis well showing the clinoforms (blue arrows) and the bright amplitude anomalies (green arrows) clearly (data courtesy of TGS, Asker, Norway).

detail. A straightforward choice for accomplishing this was to put the data through poststack impedance inversion and generate one or more discontinuity attributes such as coherence and curvature. Thus, the objectives set for the exercise were (1) to use impedance inversion to follow potential reservoir leads within the Stø (Mid-Jurassic) and Kobbe (Mid-Triassic) Formations, (2) detect the potential prospects associated with direct hydrocarbon indicators (DHIs), and (3) study the areal extent of the potential reservoirs present in the interval of interest.

A cursory examination of the 3D seismic volume (by way of vertical and horizontal sections) reveals bright amplitude anomalies in the shallow intervals, interspersed with many discontinuities interpreted as faults (Figures 4 and 5). Most of the bright amplitude anomalies appear to be coming from channels that show up well on the horizontal displays (time or horizon slices) as shown in Figure 6.

There may be several reasons for an amplitude anomaly to show up on seismic data. Besides seismic processing artifacts, a clean, high-porosity wet sand, tight sand, low-saturation gas sand, or a lateral change in lithology could exhibit a high-amplitude anomaly. Similarly, streaks of salt, volcanics, or carbonates could indicate anomalies. Needless to say, a combination of one or more of the above-stated geologic conditions could produce false amplitude anomalies. Processing of seismic data in an amplitude-friendly way and gaining good knowledge about the geology of the area under investigation together with the expected seismic response through modeling are established ways of lowering the uncertainty in the analysis.

Discriminating seismic anomalies associated with the presence of hydrocarbons from those that are not could be challenging. But it is important that such challenges are addressed to prevent costly drilling failures.

Workflow adopted

A workflow shown in Figure 7 was devised to quantify the shallow high-amplitude seismic anomalies that have been discussed above. They are described in detail and stepwise in the following sections.

Coherence attribute application

As our starting point, we decided to compute the coherence attribute so that it will provide a more accurate interpretation of the smaller as well as larger geologic features. Discontinuity attributes such as coherence enhance the edges of the features of interest and accelerate the interpretation. There are various algorithms available for comput-

Figure 5. Inline AA′ seismic section from the input seismic data. Several bright spots are seen above the horizon in black that has been picked on the data. We generate a chair display to examine the amplitudes of the bright spots indicated with green arrows as shown on the next figure (data courtesy of TGS, Asker, Norway).
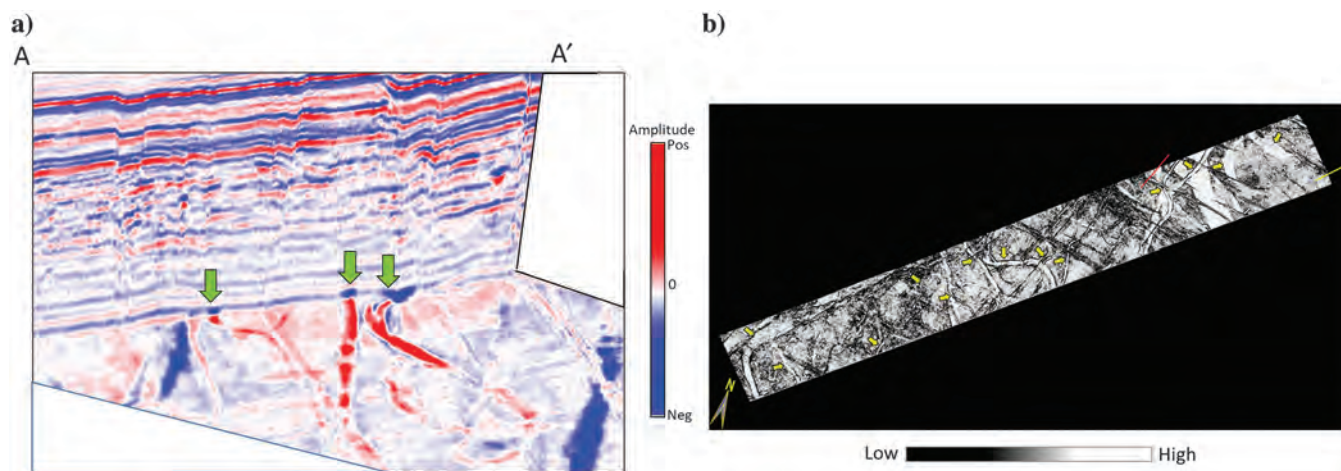
Figure 6. (a) A chair display exhibiting inline AA′ and time slice at 1312 ms from the input seismic data. The three green arrows show the high amplitudes seen in this figure, and they are seen here correlated with channel features. Besides this, several almost-vertical faults are seen on the vertical section, and their indications are corroborated on fault lineaments seen on the time slice. A horizon slice below the Stø Formation that exhibits several channels that have been marked with yellow arrows (data courtesy of TGS, Asker, Norway).

ing coherence, including crosscorrelation, semblance, eigendecomposition of covariant matrices, and a more general computation than the eigendecomposition approach called the energy-ratio method (Chopra and Marfurt, 2008). The eigendecomposition method is based on the eigenvectors and eigenvalues of the of the covariance matrix generated for the unit cube made up of the input parameters for coherence computations, and it is given as the ratio of the principal eigenvalue to the sum of all the eigenvalues or the trace of the matrix. In the energy ratio algorithm, first the energy of the coherent component of the input traces is calculated, followed by the energy of the input traces, which is the total energy. The coherence coefficient is then computed as the ratio of the energy of the coherent component to the total energy. Energy ratio coherence yields more crisp images of the discontinuity features of interest.

After preconditioning the input stacked data volume using structure-oriented filtering, we generated a coherence attribute volume using the energy-ratio algorithm. The results are clearer and crisper in comparison with the other methods. In Figure 8, we show a set of time slices at 1004, 1292, and 1332 ms. Each of these displays shows several faults with orientations in the northwest–southeast and northeast–southwest directions. In addition to the faults, several well-defined channels are also seen.

Even though our main objective is the characterization of shallow high-amplitude anomalies in the area, because the coherence attribute defines the faults and the edges of the channels very well, we overlay this attribute on the inversion attribute displays later for more effective visualization.

Spectral decomposition application as DHI indicator

Next, we explore the application of spectral decomposition to the data at hand. The decomposition of the seismic signal band into constituent frequencies is referred to as spectral decomposition. It is a useful tool that has important applications including differentiation of lateral and vertical lithologic and/or pore-fluid
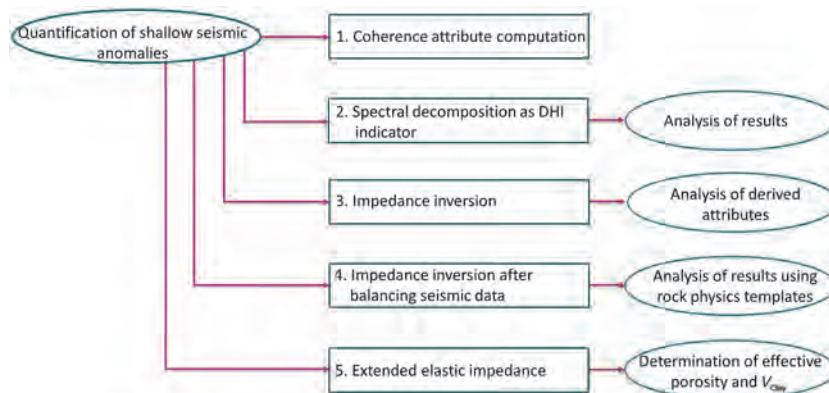

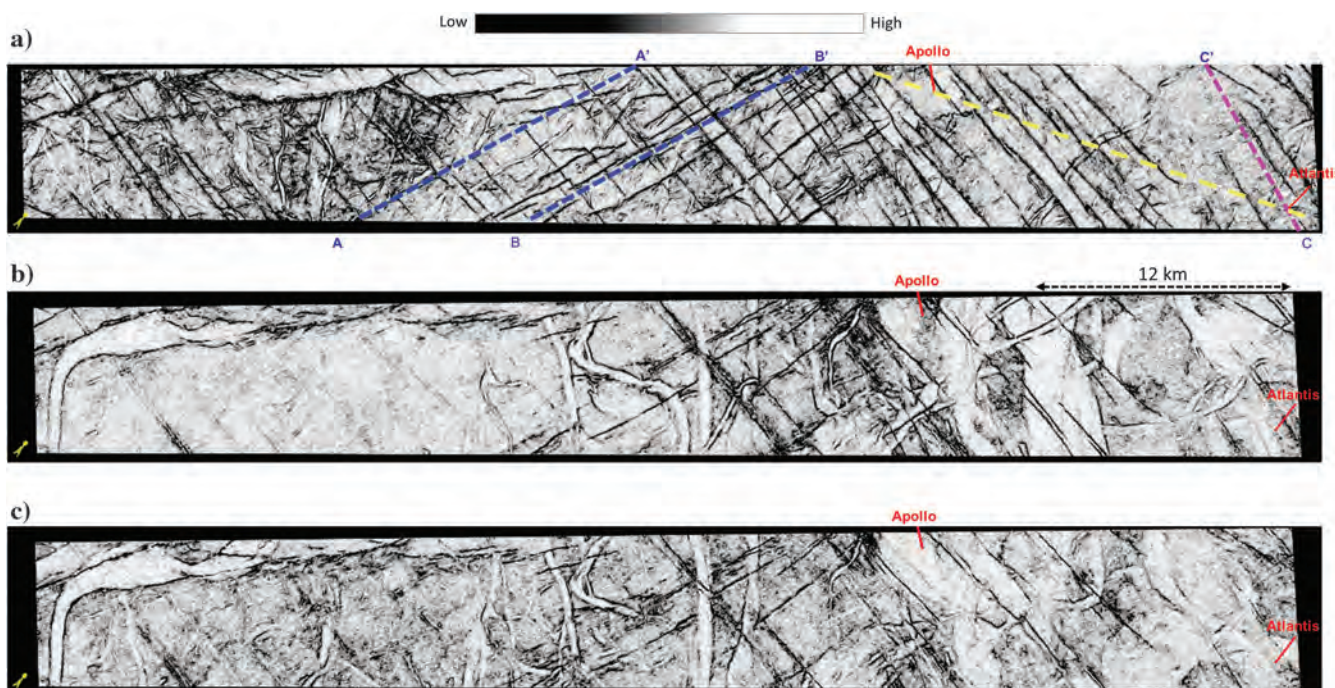**Figure 7.** Workflow adopted for discrimination of seismic anomalies.

Figure 8. Time slices from the coherence volume at (a) 1004, (b) 1292, and (c) 1332 ms. Faults with northwest–southeast and northeast–southwest orientations are seen clearly. Several paleochannels of different width are also seen at these levels. The location of the two wells, Apollo and Atlantis, are marked in red. The lines in blue marked as AA′ and BB′ are the location of the seismic sections that are displayed in subsequent figures (data courtesy of TGS, Asker, Norway).
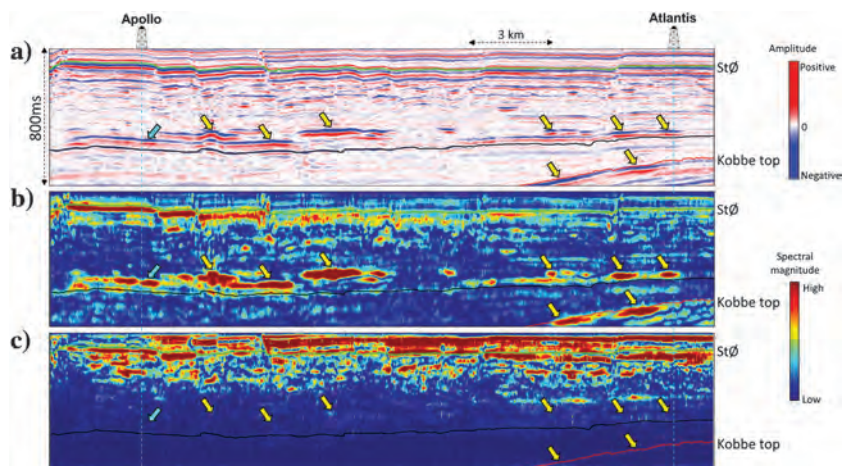
changes such as the DHI indicator and seismic geomor-phological applications aimed at delineating strati-graphic traps.

In the context of DHIs, the basic premise is that reflections from fluid-saturated rocks are frequency de-pendent (Dutta and Ode, 1983; Denneman et al., 2002). Goloshubin et al. (2006) find that such reflection coef-ficient (water/gas) ratios are three times stronger at 14 Hz than at 50 Hz, and they suggest that the observed reflection amplitudes be used for detecting liquid-satu-rated areas in thin porous layers. In the presence of hy-drocarbons, the encasing formations selectively reflect particular frequencies and not others, leading to high amplitudes on seismic sections. This is because higher frequencies suffer higher attenuation while traversing hydrocarbon reservoirs. In the event that the reservoirs are thin, the tuning of reflections also exacerbates the amplitude responses from reservoirs. Castagna et al. (2003) demonstrate that the instantaneous spectral analysis of seismic data shows that low-frequency modes of the seismic wavefield provide useful informa-tion for the study of fluid-saturated rocks.

We used the matching pursuit spectral decomposi-tion method as described by Liu and Marfurt (2007). It assumes that each band-limited seismic trace can be represented as a linear combination of either Ricker or Morlet wavelets. A wavelet dictionary is precomputed and comprises the zero phase wavelets and 90° phase wavelets with different frequencies (sampled at 0.1 Hz increments), in fact forming a complex wavelet diction-ary. Using complex trace attribute analysis, the center time for each candidate wavelet is estimated by the peaks of the amplitude in the instantaneous envelope, and its average frequency is estimated by the instanta-neous frequency at the envelope peak. A search is per-formed over the user-defined range of frequencies and time samples about the precomputed peak frequency and peak envelope to obtain the wavelet frequency-time pair that best correlates with the data. The difference be-tween the analytic seismic trace and the matched com-plex wavelets is iteratively minimized in a least-squares sense. Each wavelet is then decomposed into its spectral magnitude and phase components. The process is re-peated until the residual falls below a threshold that is considered to be the noise level. This way, the input seis-mic data are decomposed into the desired frequency components at a desired increment. To validate the de-composition, one can sum up the spectral components to reconstruct the original data. Alternatively, one can bal-ance the magnitude spectrum prior to reconstruction, re-sulting in a spectrally balanced seismic image.

On analyzing the spectral magnitude data, we noticed that many of the high-amplitude anomalies are associated with higher spectral amplitudes. In Figure 9a, we show an arbitrary line passing through the Apollo and Atlantis wells, from the input seismic volume, and we notice some high-amplitude anomalies. The location of the line is in-dicated in yellow in Figure 8a. We generate the equiv-alent spectral magnitude displays at 20 and 60 Hz, and they are shown in Figure 9b and 9c. Notice the high-spectral-magnitude values seen at 20 Hz, but not on the 60 Hz display, even though the bandwidth of the data extends to greater than 80 Hz. The Apollo well being drilled to a shallow depth does not reach the Kobbe top level, but there is a definite anomaly at the intermediate level. Thus, spectral decomposition serves as a preliminary tool for location of the high-amplitude anomalies that could be hy-drocarbon bearing, and we now proceed further to seek their confirmation.

Impedance inversion application

Well-log data are used to tie the main time horizons to the seismic data and de-fine the impedance bounds for each layer. For well-log correlation, a wavelet needs to extracted from the seismic data, which was done using a statistical process. In Figure 10, we show the well log-to-seismic correlation for the Atlantis well, with the extracted wavelet shown on top. The modeled synthetic traces generated from the impedance log are in blue and are shown correlated with the seismic traces at the location of the well in red. A reasonably good cor-relation is seen between the two. It is not 100%, and thus it lends support to our choice of wavelet extraction using a statistical process. As impedance in-

Figure 9. (a) Segment of an arbitrary line passing through the Apollo and At-lantis wells from (a) seismic data and showing high-amplitude anomalies. The display contrast has been reduced somewhat to depict these anomalies clearly. The location of the arbitrary line is indicated in yellow in Figure 8a. The equiv-alent segments of this arbitrary line extracted from 20 to 60 Hz volumes gener-ated using matching pursuit spectral decomposition, are shown in (b and c), respectively. Notice the anomalies indicated with yellow arrows exhibit high spectral magnitudes on the 20 Hz section and not on the 60 Hz section. The Apollo well being drilled to a shallow depth does not reach the Kobbe top level, but there is a definite anomaly at the intermediate level (data courtesy of TGS, Asker, Norway).

version is usually carried out in narrow time windows; the attenuation effects of the wavelet frequency are negligible, but we do account for it in the next section.

We make use of a model-based poststack impedance inversion to transform the seismic amplitude volume into an impedance volume. As the name implies, the starting model is a low-frequency impedance model that was generated using the Atlantis well that extended through the formations of interest. Horizons corresponding to the Stø and Kobbe top formations were used to constrain the low-frequency model with another pickable horizon in between, called the *intermediate* (shown in black in Figure 5). Because only one well was used for constructing the low-frequency model, the impedance within each layer may vary vertically, but it is taken as being constant laterally. In the model-based inversion process, the starting model is compared with the input seismic data, and the error between them is iteratively minimized in a least-squares sense.

A segment of the inverted P-impedance section along line CC′ (the location is displayed in Figure 8) is shown in Figure 11. Notice that the high seismic amplitudes marked in green are associated with low impedance values. We again show the high-amplitude anomalies along line BB′ in Figure 12, which also exhibits a stratal grid that is used for displaying stratal slices. The term "stratal slice" may be clarified here. The Stø horizon was used to generate another phantom horizon approximately 100 ms below it, and the interval divided into 10 proportional slices. The attribute displayed along each such proportional slice is referred to as a stratal slice. The stratal slice at the location of the blue arrow in Figure 12 is exhibited in Figure 13, which is a composite visual display of impedance and coherence attributes. Some of the channel features show low impedance values in dark blue and are indicated with light-blue arrows, and other channels show high impedance fills as indicated with pale yellow arrows. Fault signatures are seen as black coherence lineaments.

The above workflow uses low impedance for screening out high seismic anomalies, and it may not be sufficient for distinguishing bright amplitude anomalies associated with hydrocarbons from other geologic elements. For analyzing these, we turned to the well-log

data for the Atlantis well in which dipole sonic and density curves were available, and after computing different attributes such as Lambda-rho and Mu-rho (Goodway et al., 1997), we crossplotted them. On the Lambda-rho versus Mu-rho crossplot (Figure 14), we noticed that gas sand in the Snadd Formation exhibited low values of Lambda-rho and somewhat higher values of Mu-rho.
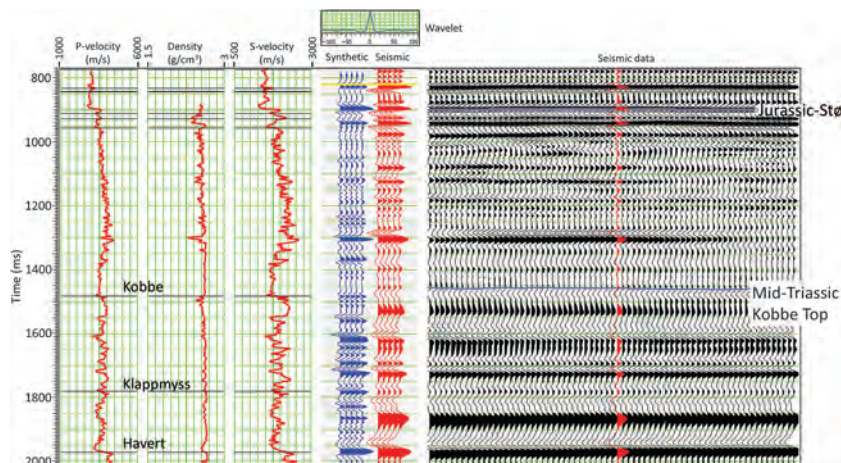
Figure 10. Well-to-seismic tie for Atlantis well. The wavelet extracted from the seismic data is shown above. The traces in blue are the modeled traces, and the seismic traces at the location of the well are in red.
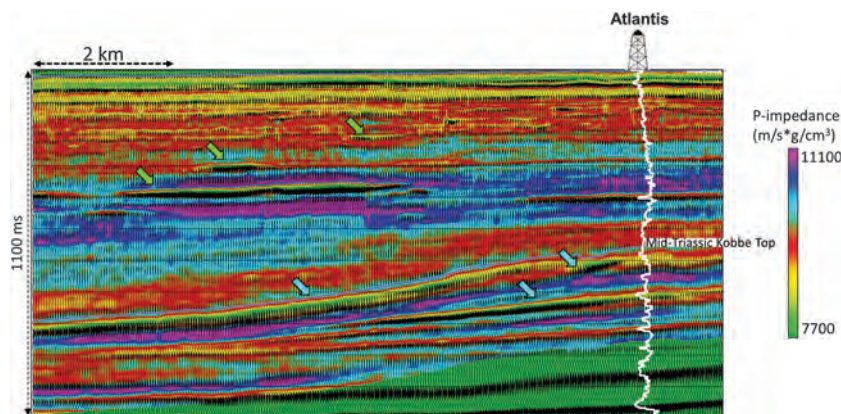
Figure 11. Inverted P-impedance section with seismic overlay along crossline CC′ passing through well Atlantis and displayed in Figure 8. The log curve overlaid in white is the computed P-impedance. The high seismic amplitudes marked in green are seen to be associated with lower impedance values (data courtesy of TGS, Asker, Norway).
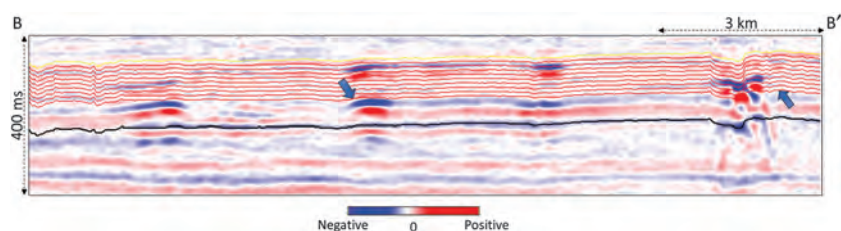
Figure 12. Inline BB′ with the overlay of the stratal slice grid. The stratal slice displayed in Figure 13 is indicated with blue arrows.

Besides, there was an overlap between the points representing the gas sand and those coming from the Jurassic-Stø and Mid-Triassic Kobbe Formations. But by bringing density into our analysis, it was possible to discriminate between them. Thus, to extract Lambda-rho, Mu-rho, and density volumes from seismic data, we decided to run prestack simultaneous impedance inversion, in which multiple partial offset or angle substacks are inverted simultaneously. For each angle stack, a unique wavelet was estimated from seismic data using a statistical process. The extracted wavelets and their individual frequency spectra are shown in Figure 15. Prior to offset-to-angle domain conversion, the prestack seismic data in the form of offset gathers were preconditioned by way of background noise removal and trim static to enhance the S/N. Subsurface low-frequency models for P-impedance, S-impedance, and density, constrained with the appropriate horizons in the broad zone of interest, are constructed using the dipole sonic and density log data available for the Atlantis well.

The simultaneous inversion process begins with the low-frequency model, which is used to generate synthetic traces for the input partial angle stacks. Zoeppritz equations, or their approximations, are used to estimate the band-limited elastic reflectivities. The angle-dependent wavelets are convolved with the modeled reflectivities for generating synthetic traces, which are then compared with corresponding real data traces. The model impedance values are iteratively tweaked in such a manner that the mismatch between the modeled angle gather and the real angle gather is minimized in a least-squares sense. Because a different wavelet is extracted for each partial angle stack and used in the inversion, the angle-dependent amplitude information in the gather is used.

Once the background models, wavelets, and partial stacks were obtained, inversion analysis was carried out at the Apollo and Atlantis wells, which allows the optimization of the inversion parameters and validation. After performing it at well locations and obtaining satisfactory results, prestack simultaneous inversion was run for the full volume to extract P-impedance, S-impedance, and density volumes. Even though it is an arduous task to extract density from seismic data due to the unavailability of noise-free long-offset data, we could extract it as the angle range for the available data extended to 47°–48°. Once we had the impedance volumes, Lambda-rho and Mu-rho attributes were generated and then we examined the anomalies in the Lambda-rho-Mu-rho crossplot space.

The Lambda-rho and Mu-rho analysis is based on the assumption that Lamé's first constant, Lambda (which is a proxy for incompressibility) is sensitive to pore fluid in the rock, and the other constant Mu (the modulus of rigidity) is only influenced by the matrix material. Because gas is compressible, for a gas sand, Lambda should be low, and Mu
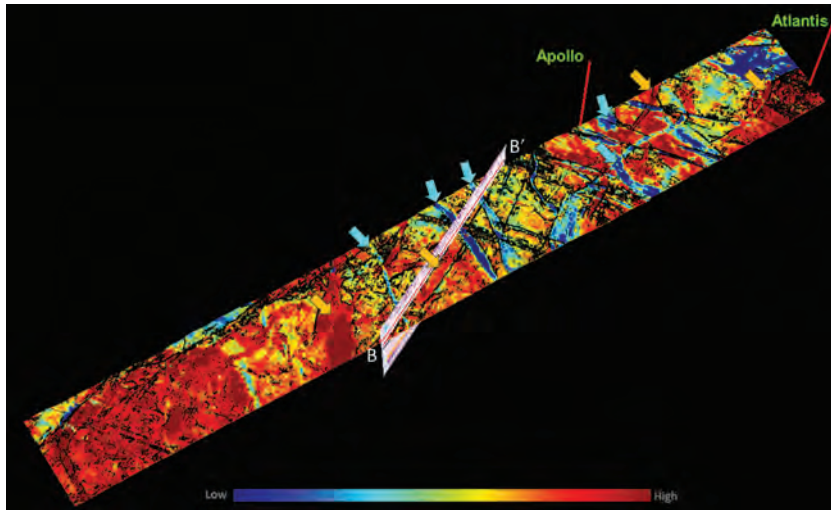
Figure 13. Stratal slice as indicated in Figure 12 from the impedance volume with the overlay of energy-ratio coherence. Notice the low impedance in blue seen in the channels indicated with cyan arrows and high impedance indicated with pale yellow arrows. Inline BB′ shown in the previous slide is also included in the display (data courtesy of TGS, Asker, Norway).
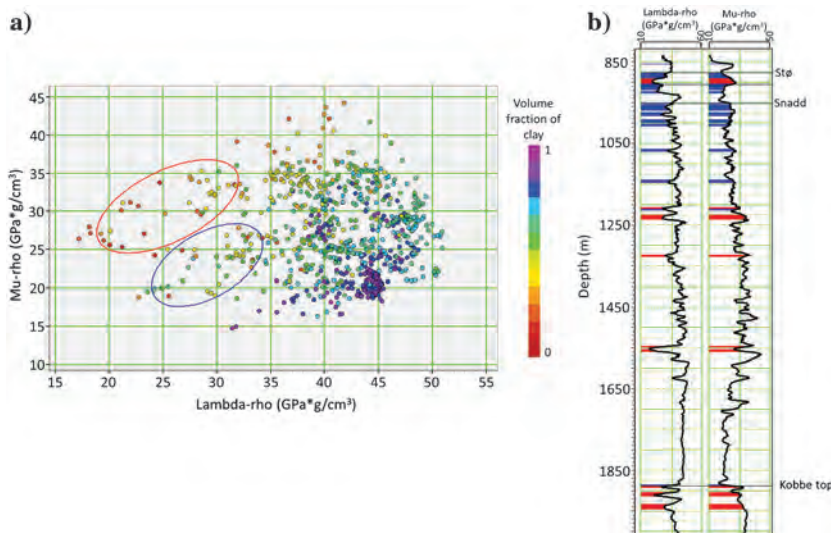
Figure 14. Crossplot of Lambda-rho versus Mu-rho for the interval spanning the Stø to Kobbe Formations. The cluster points are color coded with the fraction of volume clay. Cluster points enclosed in red (low Lambda-rho and high Mu-rho) and blue (low Lambda-rho and moderate Mu-rho) polygons are back-projected and are seen to be coming from the Kobbe Formation and the Snadd Formation, with some overlap as well in between.

should be high (quartz is more rigid than shale). Thus, for a gas sand, we expect them to exhibit low values of Lambda-rho and high values of Mu-rho.

In Figure 16, we show segments of Lambda-rho and Mu-rho sections passing through the Atlantis well, and with the respective well-log curves overlaid. We notice two zones that stand out exhibiting low Lambda-rho and high Mu-rho, and they are highlighted in black. These indications are suggestive that they represent prospective zones. We take this analysis forward through crossplotting the two attributes (Lambda-rho and Mu-rho) and picking up a cluster corresponding to low Lambda-rho and high Mu-rho enclosed in Lamé red polygon and shown in Figure 17a. On back-projecting these enclosed points on the vertical (Figure 17b), we see the variation in the two zones that we have considered prospective.

A similar feasibility analysis was carried out for an inline passing through the Apollo well. Again, picking up the high-amplitude anomalies on seismic, examining them in the Lambda-rho versus Mu-rho crossplot space, and back-projecting them on the vertical section, we saw only the anomalies at the lower level as being prospective. We therefore concluded that all the high-amplitude anomalies seen on the seismic data may not be associated with hydrocarbons, and we need to examine them with a different approach.

Because we were able to extract the density attribute also, in Figure 18 we show the density section equivalent to the Lambda-rho and Mu-rho sections shown in Figure 16. Notice that the low-density anomaly is indicated with the yellow arrow, but no density anomaly is seen at the lower level (the pink arrow). Next, we crossplot density versus P-impedance as shown in Figure 19a for the line passing through the Atlantis well, and after enclosing the cluster points exhibiting low density and low impedance, and back-projecting, only the anomaly at the yellow arrow is seen highlighted as shown in Figure 19b. We therefore conclude that we can trust this anomaly as being associated with hydrocarbons.

Thus, by adopting a workflow that entails the generation of P-impedance, S-impedance, and density attributes and examining these attributes first in the Lambda-rho versus Mu-rho crossplot space, and then in the P-impedance versus density crossplot space, it is possible to identify the fluid-associated anomalies.

Impedance inversion after frequency balancing of seismic data and analysis using RPTs

As we noticed in Figure 15, the spectra for the wavelets extracted from the near-, mid-, and far-angle stacks exhibit a lowering in frequency content as we go from the near- to far-angle stack, via the mid-angle stack, as well as an overall roll off on
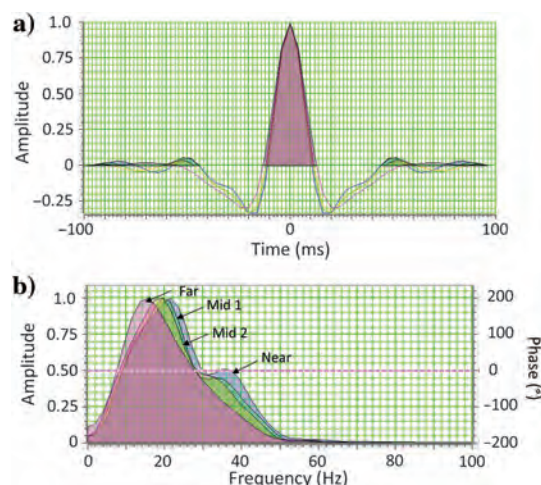

Figure 15. (a) Wavelets extracted the near-, mid-, and far-angle stacks; (b) frequency spectra for the wavelets extracted in (a). Notice the gradual reduction in the frequency content in going from the near- to the far-angle stack wavelets, as well as the roll-offs on the higher frequency side.
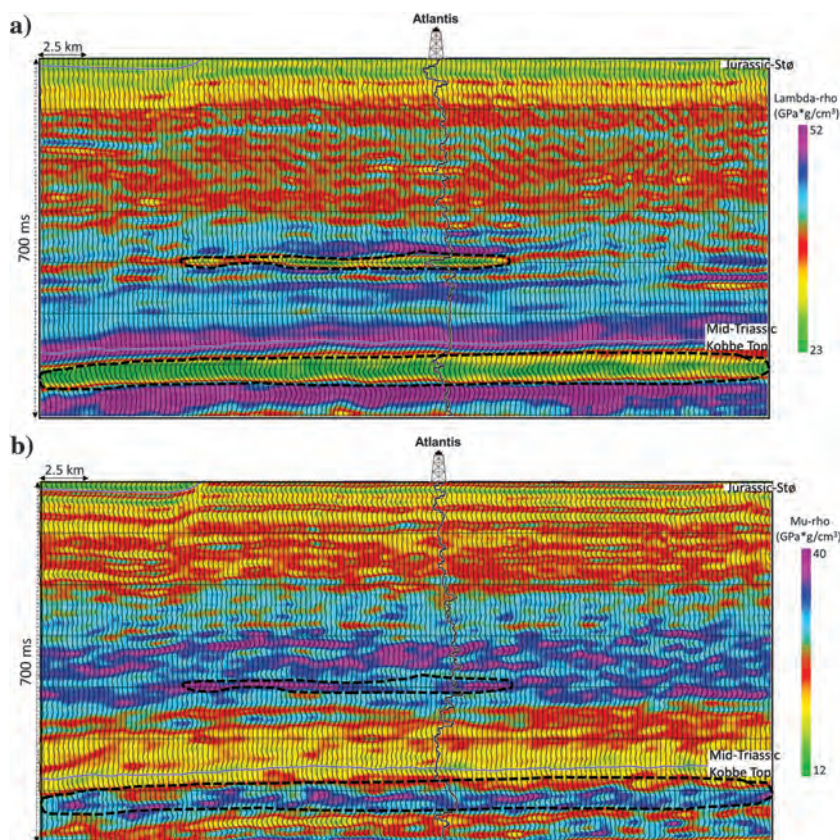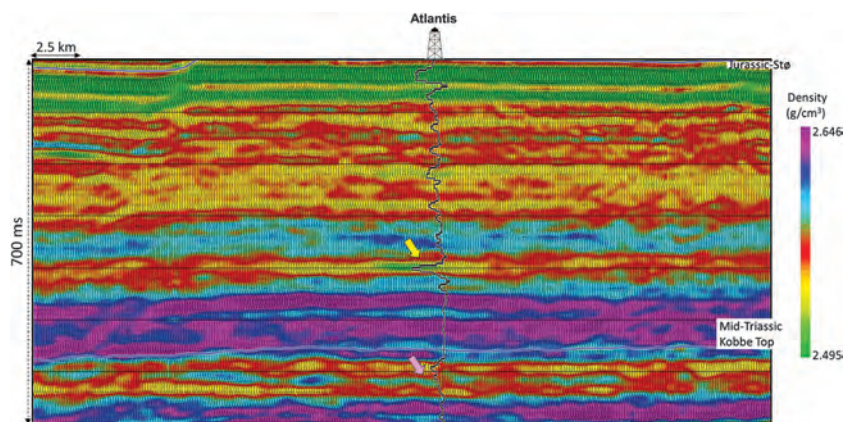

Figure 16. Equivalent segments of sections passing through Atlantis well from (a) Lambda-rho and (b) Mu-rho attributes generated using prestack simultaneous inversion. The individual curves overlaid are the Lambda-rho and Mu-rho log curves on the respective sections. Notice the good correlation between the measured and inverted attributes (data courtesy of TGS, Asker, Norway).
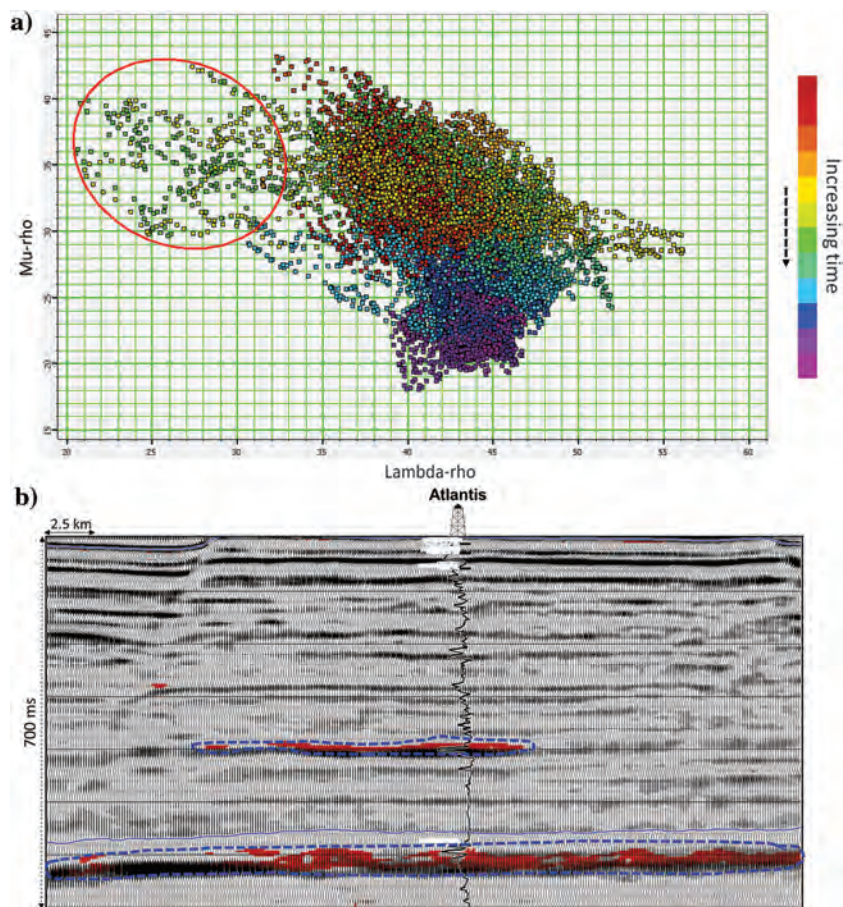
Figure 17. (a) Crossplot between Lambda-rho and Mu-rho attributes from the impedance sections shown in Figure 16 passing through the Atlantis well. Although a high density of points form a cluster in the middle of the crossplot, there are some points that form a cluster deviating from it. These points represent low values of Lambda-rho and high values of Mu-rho, which could be considered as representing prospective sandstones probably impregnated with gas. These points are enclosed in a red polygon as shown and back-projected onto the vertical section as shown in (b). Notice the points are coming from two different levels (red paintbrush patterns enclosed in dashed blue lines).

Figure 18. Equivalent segment of the profiles shown in Figure 16 passing through the Atlantis well, extracted from the density volume that is generated using prestack simultaneous inversion. The density log curve is overlaid on the section. Notice the good correlation between the measured and inverted density attribute (data courtesy of TGS, Asker, Norway).

the higher frequency side. These effects are a manifestation of the offset/angle dependent attenuation as well as the changes in the seismic wavelet with time/depth. We decided to compensate for this by balancing or flattening the spectra of the near-, mid-, and far-angle stack and bringing it to the same level. Our method of choice for this application was the thin-bed reflectivity inversion, which has been described and illustrated elsewhere (Chopra et al., 2006; Puryear and Castagna, 2008). In this process, the time-varying effect of the propagating wavelet is removed from the seismic data and the output of the spectral inversion process can be viewed as spectrally broadened seismic data, retrieved in the form of broadband reflectivity that can be filtered back to any desired bandwidth. This usually represents useful information for interpretation purposes. Filtered thin-bed reflectivity, obtained by convolving the reflectivity with a wavelet of a known frequency band-pass, not only provides an opportunity to study reflection character associated with features of interest, but it also serves to confirm its close match with the original data. In Figure 20, we show the equivalent wavelets extracted from the same time window after frequency balancing. Prestack simultaneous impedance inversion carried out with these wavelets and the balanced near-, mid-, and far-angle stack yield higher resolution and thus lead to more accurate interpretation. In Figure 21, we show the line CC′ from the P-impedance volumes before and after the balancing of the frequency spectra for the wavelets extracted from the near-, mid-, and far-angle stacks. Notice the crisper look of the anomalies as well as other events and their better standout seen on the sections after frequency spectra balancing.

Using RPTs

Ødegaard and Avseth (2004) introduce the use of RPTs as an aid in interpretation of lithology and pore fluid interpretation of well-log data and elastic inversion results. Since then, RPTs have become an effective tool for delineation of lithology and fluid content, a visual integration of well-log and seismic data and their calibration, leading to quantitative interpretation. Instead of defining arbitrary cut-off values for pro-

spective intervals, RPTs help us define an accurate zone(s) for them.

These templates are first constructed or modeled from well-log data, using theoretical rock-physics principles for generation of trends for different lithologies and fluids that may be expected in the area. Once these are generated, they are used as an aid or guide for interpretation of elastic inversion-derived attributes.

The well-log data measured in the Atlantis, well together with the petrophysical analysis carried out on it, furnished the data required for generation of the RPTs being used in this exercise.

The starting point for the generation of RPTs for the interval of interest is the petrophysical analysis for calculation of lithologic and fluid composition, as well as the porosity in the Atlantis well. The next step is the generation of porosity trends for the lithologies of interest, usually based on the Hertz-Mindlin contact theory (Mindlin, 1949) for pressure dependence of porosity (Ødegaard and Avseth, 2004). The porosity values range from no porosity to the maximum porosity expected in the interval, of course using the bulk and shear moduli of the solid mineral comprising the dry rock. Between end values of porosity, the moduli for the dry rock are estimated based on the Hashin Shtrikman (HS) bounds (Hashin and Shtrikman, 1963) that allow the prediction of the effective elastic moduli of a mixture of grains and pores. The lower HS bound applies for unconsolidated rocks, whereas cemented rocks are governed by the upper HS bound, both cases assuming isotropic and elastic rocks.

Finally, the dry rock parameters computed in the previous two steps are input into Gassmann's equations to calculate saturated rock properties for brine and hydrocarbons. In the present exercise, the reservoir fluid is water, gas, or their mixture. These computations allow us to determine P-velocity, S-velocity, and density, and thus P-impedance and V_P-V_S ratio, which are the typical output attributes from seismic elastic impedance inversion.

In Figure 22a, we show an RPTs overlaid on the crossplot between the P-impedance and V_P-V_S ratio for the Atlantis well, for the interval between Stø and the Havert Formations. The cluster points are color coded with porosity values ranging from 5% to 25%. The clusters of points with low impedance and low V_P-V_S ratio exhibit high porosity and high gas saturation and are enclosed in red and purple polygons. When back-projected on to the
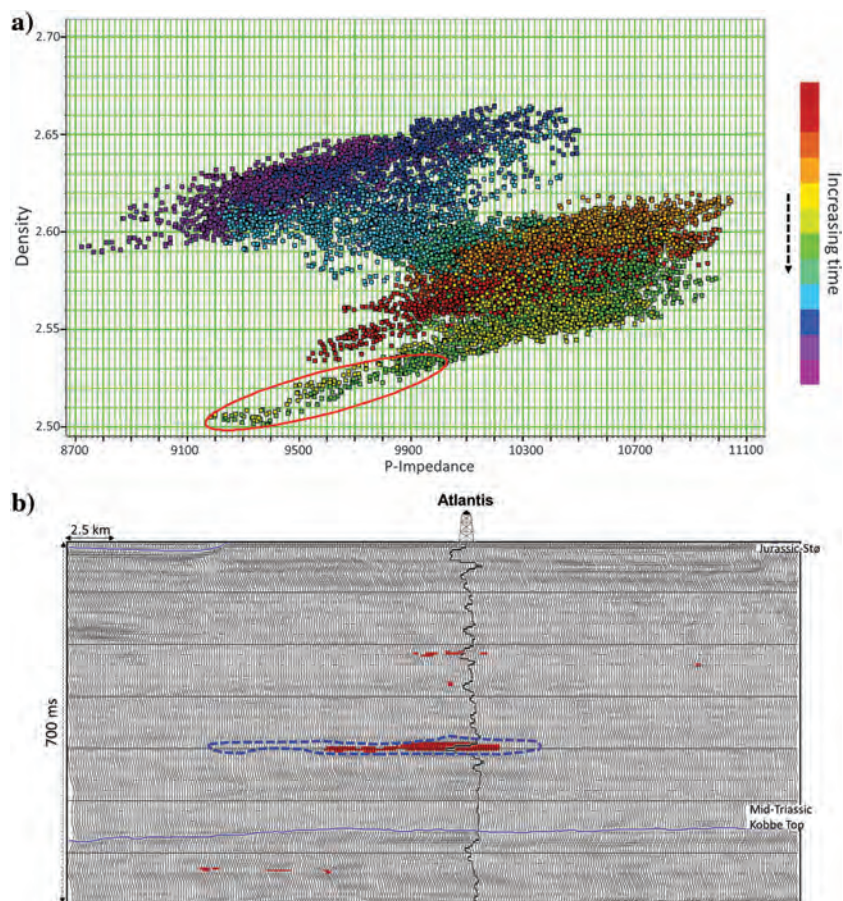
Figure 19. (a) Crossplot between the inverted density and P-impedance attributes derived from the prestack simultaneous impedance inversion. The cluster of points enclosed in the red polygon exhibit low density and low impedance and so could represent hydrocarbon fluids. On back-projecting these points on the vertical section as shown in (b), they highlight only the anomaly at the upper level, and not the lower one.
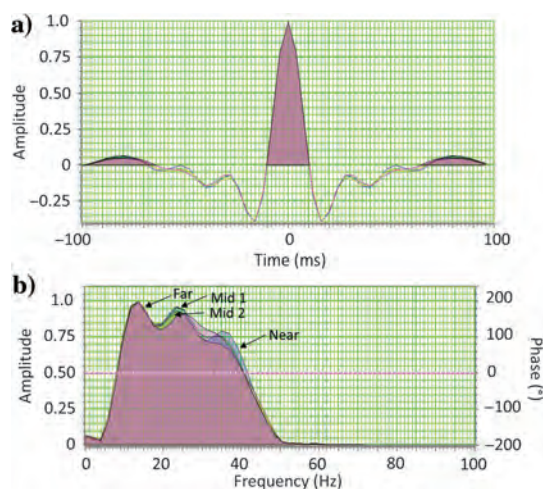
Figure 20. (a) Wavelets extracted the near-, mid-, and far-angle stacks and (b) frequency spectra for the wavelets extracted in (a). Notice the balancing of the frequency content for the near-, mid-, and far-angle stack wavelets.

well-log curves as shown in Figure 22b, they highlight the intervals between the Stø and Kobbe markers.

In Figure 22c, we show a similar crossplot for the P-impedance and V_P-V_S ratio derived from prestack simultaneous impedance inversion without frequency balancing, with overlaid RPTs. Notice that the cluster of points has an overall shape that is similar to the one seen in the crossplot shown in Figure 22a from the Atlantis well. The drawback we see is that the cluster points within the red and purple polygons are not spread out. In Figure 22d, we show an equivalent crossplot from the two attributes derived from prestack simultaneous impedance inversion with frequency balancing. Now we see a good spread of cluster points within the red and purple polygons. On backtracking the cluster polygons within the different polygons on vertical seismic (Figure 23), we note that they highlight the high-amplitude anomalies at the Stø, Snadd, and Kobbe levels, which we have seen before.

EEI application

After application of spectral decomposition as DHI and prestack simultaneous impedance inversion, we decided to further quantify the hydrocarbon bearing zones in our broad zone of interest. We pursue this exercise with the application of the EEI approach.

Elastic impedance inversion is a generalization of acoustic impedance for a variable angle of incidence, and it provides a consistent and absolute framework to calibrate and invert non-zero-offset seismic data (Con-

nolly, 1999) for fluid discrimination and lithology prediction for reservoirs. However, the elastic impedance values decrease with the increasing angle of incidence and require a scale factor varying angles if they were to be compared with acoustic impedance values. Whitcombe (2002) not only introduces normalizing constants to remove the variable dimensionality and overcame this problem, but also introduces EEI (Whitcombe et al., 2002), which broadens the definition of elastic impedance. According to this formulation, some of the rock properties cannot be predicted by the elastic impedance approach that usually considers the angle of incidence range as 0°–30°, which are the values taken by $\sin^2 \theta$. Consequently, by bringing about a change of variable, i.e., $\sin^2 \theta$ replaced with $\tan \chi$, the angle range is extended from −90° to +90°, and this allows calculation of an impedance value beyond physically observable range of angle θ. The χ angle can be selected to optimize the correlation of the EEI curves with petrophysical reservoir parameters, such as V_{clay}, water saturation, and porosity or with elastic parameters such as bulk modulus, shear modulus, Lamé constants, and so on. It may be noted that χ is not the actual reflection angle, but it is an independent input variable that is required for computing EEI.

We illustrate the different steps followed in the EEI approach in Figure 24a. Because EEI reflectivities are crosscorrelated with desirable V_{clay} and effective porosity log curves for different values of the angles, the correlation coefficients are plotted in Figure 24b. The maximum positive correlation coefficient of 0.85 for V_{clay} (green curve) is seen at an angle of 28°, and a negative correlation coefficient of 0.9 at an angle of 22° (blue curve). The values of angles allow the determination of these properties (effective porosity and V_{clay}) from seismic data through the application of Zoeppritz equations on seismic angle gathers.

In Figure 25a and 25b, we exhibit equivalent crossline sections from the effective porosity and V_{clay} volumes with the respective petrophysical log curves overlaid on them. A reasonably good match between them is seen in both cases, which enhances our confidence in the application of the followed approach for the data at hand.

Next, we crossplotted the effective porosity and V_{clay} derived attributes as shown in Figure 26a. On enclosing the cluster of points that exhibit high porosity and low values or not-so-low values of V_{clay} with red, green, and blue polygons, and back projecting on the vertical seismic, we are able to highlight these points coming from different zones. In Figure 26b, we see the differentiation of the potential reservoirs within the three
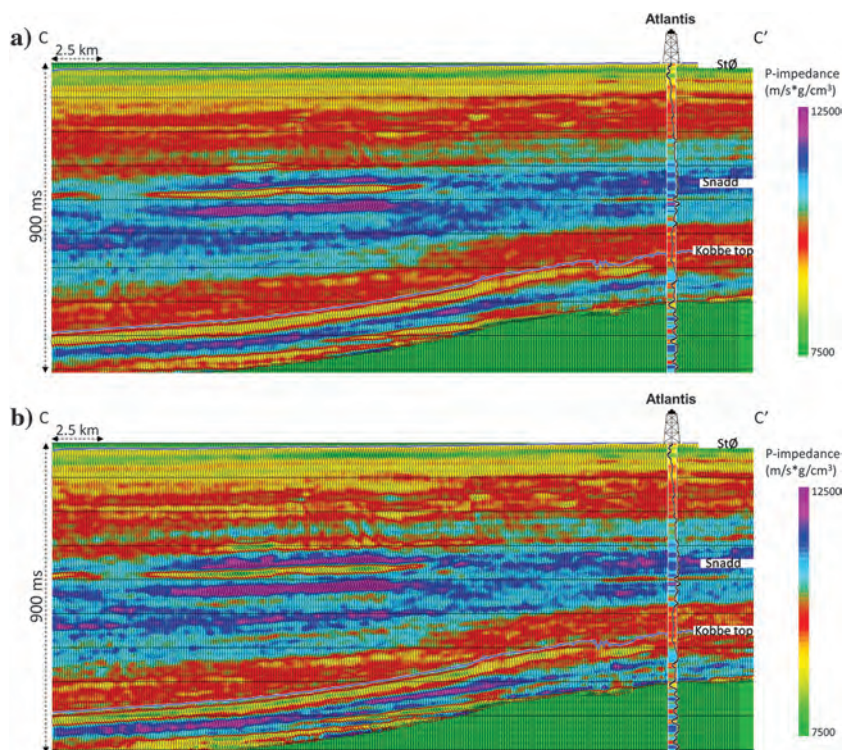
Figure 21. Inline CC′ from the P-impedance volumes: (a) before and (b) after frequency balancing of the near-, mid-, and far-angle stacks. Notice the crisper look of the anomalies as well as other events and their better stand-out seen on the sections after frequency balancing.

formations of interest, namely, the Stø, Snadd, and Kobbe Formations.

All these attribute volumes generated earlier, together with porosity and V_{clay} data volumes helped us generate displays at the levels of interest. This was a significant aid in studying the areal extent of the potential reservoirs present in the intervals of interest, which was the third objective for our exercise.

Future directions

Besides improving the quality of the existing seismic data through reprocessing (with the latest algorithms) and their integration with borehole data, the state-of-the-art acquisition of fresh data with
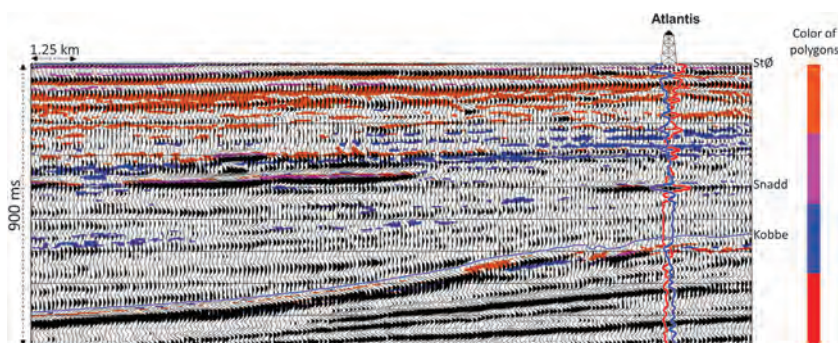
Figure 23. The cluster of points enclosed in four different polygons seen in Figure 22 back-projected on the vertical seismic section. Notice the anomalies seen at the Kobbe, Snadd, and Stø levels highlighted with purple and yellow.
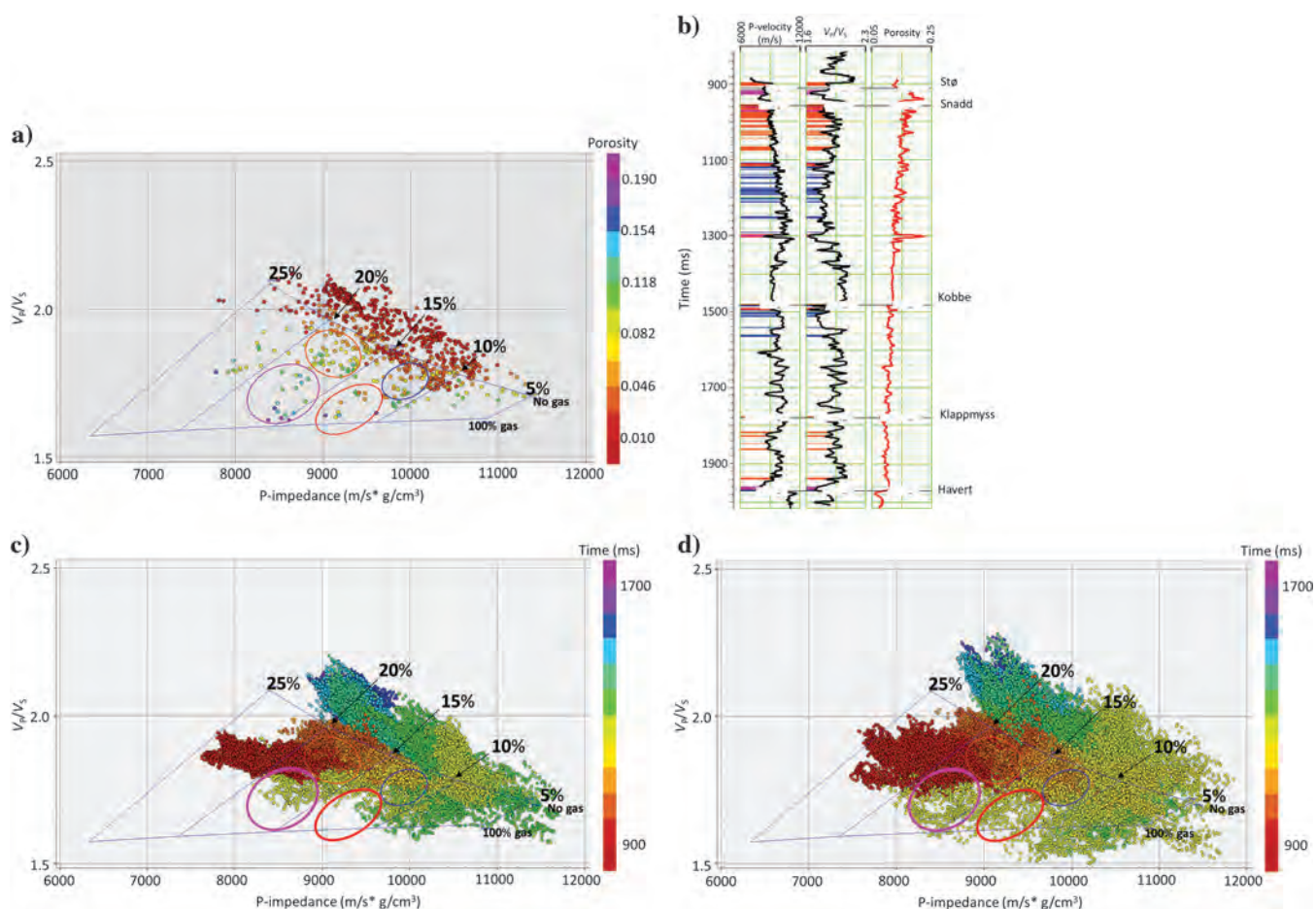
Figure 22. (a) Crossplot between the P-impedance and V_P-V_S ratio for data from Atlantis well, and for the interval between the Stø and Kobbe markers, with an RPTs overlaid on it. The cluster of points with low impedance and low V_P-V_S ratio exhibit high porosity and high gas saturation and are enclosed in red and purple polygons. When back-projected onto the well-log curves as shown in (b), the highlight the intervals between Stø and Kobbe markers, (c) Crossplot between the P-impedance and V_P-V_S ratio derived from seismic prestack simultaneous impedance inversion before frequency enhancement, and for the interval between the Stø and Kobbe markers. The same RPTs shown in (a) is overlaid on it. The cluster of points exhibit an overall shape similar to the cluster we see for well data, but they do not seem scattered enough within the red and purple polygons, (d) Crossplot between the P-impedance and V_P-V_S ratio derived from seismic prestack simultaneous impedance inversion after frequency enhancement, and for the interval between the Stø and Kobbe markers. The same RPTs shown in (a) is overlaid on it. The cluster of points exhibit an overall shape similar to the cluster we see for well data, but they are now well-scattered within the red and purple polygons, and thus they offer a more accurate interpretation.

more powerful acquisition technology are being carried out in the Barents Sea.

Among the more powerful 3D marine seismic data acquisition technologies available in the industry today, the patented P-cable multistreamer seismic system holds promise in terms of resolution on the processed data that is much greater than conventional 3D seismic data. The P-cable seismic data acquisition technology is a seismic method that uses the sensitivity of the seismic wave velocity and density of the medium for generating the data. The controlled-source electromagnetic method measures the electrical conductivity of the medium and serves as an independent source of information generating a volume of subsurface resistivity that can help locate pockets of hydrocarbon fluids. In that sense the two are disparate exploration techniques, in which the processed data are interpreted separately and the results integrated.

Natural hydrocarbon seepage on the seafloor could be due to vertical leakage of light oil or gas from charged reservoirs in the subsurface or a result of hydrocarbons that have traveled long lateral distances through vents or via porous zones or faults and reached the seafloor. Such seepage out of the seafloor can alter the physical and biological characteristics of the water-bottom sediments. Sometimes the seepage of light hydrocarbons may not be physically detected, but as they diagenetically alter the rocks or shallow sediments through which they pass, they can be detected chemically. If such seepage is physically detected on the seafloor, it could serve as a DHI. Therefore, multibeam seafloor mapping and sampling is being done by some of the operators in that area. Plans are also underway for integrating all this data for mitigating exploration risk.


Figure 24. (a) Workflow for the EEI approach for predicting the volume of petrophysical properties from seismic data, (b) crosscorrelation analysis for effective porosity (blue curve) and V_{clay} (green curve) with EEI curves. A maximum negative correlation is seen for effective porosity at 22°, and a maximum positive correlation is seen for V_{clay} at 28°.
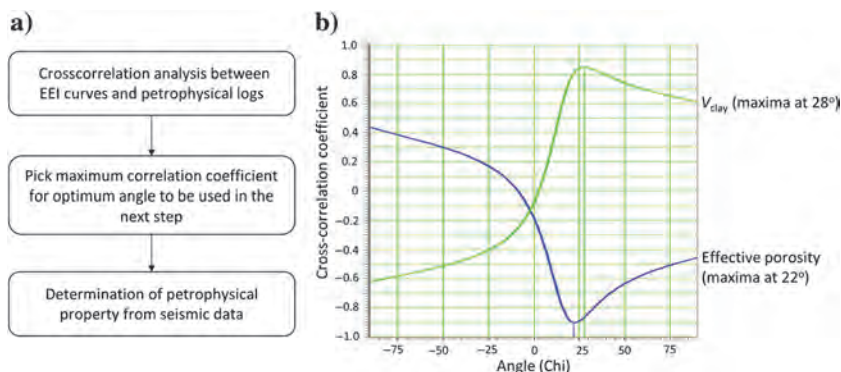
Figure 25. (a) A crossline section from inverted effective porosity volume passing through a well. The overlaid effective porosity curve shows a strong correlation with inverted results. (b) Equivalent crossline section from inverted V_{clay} volume passing through a well. The overlaid V_{clay} curve shows a strong correlation with inverted results (data courtesy of TGS, Asker, Norway).
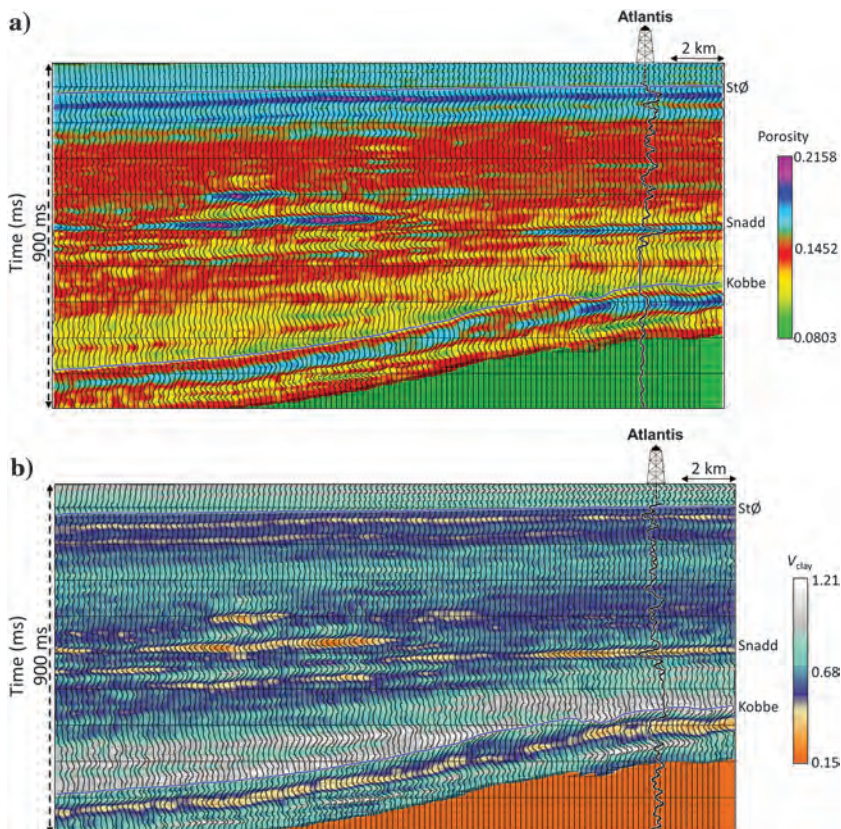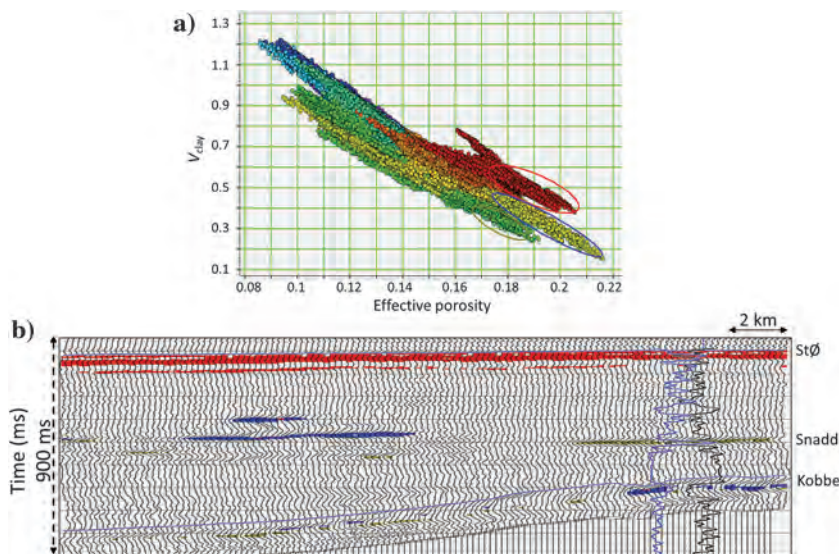
Figure 26. (a) Crossplot of inverted effective porosity and V_{clay} volumes over the zone of interest. The clusters of points exhibiting high porosity and low V_{clay} values are enclosed by red, green, and blue polygons. The back-projection of these polygons on the seismic crossline is shown in (b). Notice that we are able now to differentiate the potential reservoirs within the Stø, Snadd, and Kobbe Formations.

Conclusion

We have tried to characterize shallow bright amplitude anomalies with the application of an extensive workflow that includes attribute applications such as coherence, spectral decomposition, prestack simultaneous impedance inversion, and EEI. This has allowed us to discriminate between the bright amplitude anomalies that may be prospective from others that could be exhibiting high amplitudes due to geologic conditions. Although matching pursuit spectral decomposition helped us detect the signature of hydrocarbon-bearing anomalies at low frequencies, the P-impedance, S-impedance, and density attributes derived from simultaneous impedance inversion on analysis in crossplot space helped us high grade the anomalies pertaining to hydrocarbon presence.

We quantified our anomaly analysis in P-impedance versus V_P-V_S ratio crossplot space with overlaid RPTs as well as generation of petrophysical properties such as porosity and V_{clay} volumes through application of EEI. Those high-amplitude seismic anomalies exhibiting low-frequency signatures, low Lambda-rho and high Mu-rho, low-density and low P-impedance, high porosity, low V_{clay} fraction were considered prospective. Those anomalies that have been consistently highlighted with the different techniques used elevate the level of our confidence in their interpretation.

The overall success of such a workflow would depend on the quality of the well and seismic data used. Besides, the availability of shear log data is desirable for getting good results from simultaneous inversion, which even these days are not available.

Acknowledgments

References

Bünz, S., and S. Chand, 2013, Arctic gas-hydrates on the Svalbard margin and in the Barents Sea: 73rd Annual International Conference and Exhibition, EAGE, Extended Abstracts, doi: 10.3997/2214-4609.20131161.

Bünz, S., A. Plaza-Faverola, S. Hurter, and J. Mienert, 2014, 4D seismic study of active gas seepage systems on the Vestnesa Ridge, offshore W-Svalbard: EGU General Assembly Conference Abstracts, 16026.

Bünz, S., S. Polyanov, S. Vadakkepuliyambatta, C. Consolaro, and J. Mienert, 2012, Active gas venting through hydrate-bearing sediments on the Vestnesa Ridge, offshore W-Svalbard: Marine Geology, **332**, 189–197.

Castagna, J. P., S. Sun, and R. W. Siegfried, 2003, Instantaneous spectral analysis: Detection of low-frequency shadows associated with hydrocarbons: The Leading Edge, **22**, 120–127, doi: 10.1190/1.1559038.

Chand, S., T. Thorsnes, L. Rise, H. Brunstad, D. Stoddart, R. Bøe, P. Lågstad, and T. Svolsbru, 2012, Multiple episodes of fluid flow in the SW Barents Sea (Loppa High) evidenced by gas flares, pockmarks and gas hydrate accumulation: Earth and Planetary Science Letters, **331–332**, 1–370.

Chopra, S., J. P. Castagna, and O. Portniaguine, 2006, Seismic resolution and thin-bed reflectivity inversion: CSEG Recorder, **31**, 19–25.

Chopra, S., and K. J. Marfurt, 2008, Gleaning meaningful information from seismic attributes: First Break, **26**, 43–53, doi: 10.3997/1365-2397.2008012.

Connolly, P., 1999, Elastic impedance: The Leading Edge, **18**, 438–452, doi: 10.1190/1.1438307.

Denneman, A. I. M., G. G. Drijkoningen, D. M. J. Smeulders, and K. Wapenaar, 2002, Reflection and transmission of waves at a fluid/porous-medium interface: Geophysics, **67**, 282–291, doi: 10.1190/1.1451800.

Dutta, N. C., and H. Ode, 1983, Seismic reflections from a gas water contact: Geophysics, **48**, 148–162, doi: 10.1190/1.1441454.

Faleide, J. I., S. T. Gudlaugsson, and G. Jacquart, 1984, Evolution of the western Barents Sea: Marine and Petroleum Geology, **1**, 123–150, doi: 10.1016/0264-8172(84)90082-5.

Faleide, J. I., F. Tsikalas, A. J. Breivik, R. Mjelde, O. Ritzmann, O. Engen, J. Wilson, and O. Eldholm, 2008, Structure and evolution of the continental margin of Norway and Barents Sea: Episodes, **31**, 82–91.

Gabrielsen, R. H., R. B. Færseth, L. N. Jensen, J. E. Kalheim, and F. Riis, 1990, Structural elements of the

Norwegian continental shelf. Part I: The Barents Sea region: Norwegian Petroleum Directorate Bulletin, **6**, 47.

Glørstad-Clark, E., J. I. Faleide, B. A. Lundschien, and J. P. Nystuen, 2010, Triassic seismic sequence stratigraphy and paleogeography of the western Barents Sea Area: Marine and Petroleum Geology, **27**, 1448–1475, doi: 10.1016/j.marpetgeo.2010.02.008.

Goloshubin, G., C. Van Schuyver, V. Korneev, D. Silin, and V. Vingalov, 2006, Reservoir imaging using low frequencies of seismic reflections: The Leading Edge, **25**, 527–531, doi: 10.1190/1.2202652.

Goodway, B., T. Chen, and J. Downton, 1997, Improved AVO fluid detection and lithology discrimination using Lame petrophysical parameters: '$\lambda\rho$', '$\mu\rho$', & 'λ/μ' fluid stack' from P and S inversions: 67th Annual International Meeting, SEG, Expanded Abstracts, 183–186.

Hashin, Z., and S. Shtrikman, 1963, A variational approach to the theory of elastic behavior of multiphase materials: Journal of the Mechanics and Physics of Solids, **11**, 127–140, doi: 10.1016/0022-5096(63)90060-7.

Liu, J. L., and K. J. Marfurt, 2007, Instantaneous spectral attributes to detect channels: Geophysics, **72**, no. 2, P23–P31, doi: 10.1190/1.2428268.

Mindlin, R. D., 1949, Compliance of elastic bodies in contact: Journal of Applied Mechanics, **16**, 259–268.

Ødegaard, E., and P. Avseth, 2004, Well log and seismic data analysis using rock physics templates: First Break, **23**, 37–43.

Plaza-Faverola, A., S. Bünz, and J. Mienert, 2011, Repeated fluid expulsion through sub-seabed chimneys offshore Norway in response to glacial cycles: Earth and Planetary Science Letters, **305**, 297–308, doi: 10.1016/j.epsl.2011.03.001.

Puryear, C. I., and J. P. Castagna, 2008, Layer-thickness determination and stratigraphic interpretation using spectral inversion: Theory and application: Geophysics, **73**, no. 2, R37–R48, doi: 10.1190/1.2838274.

Whitcombe, D., 2002, Elastic impedance normalization: Geophysics, **67**, 60–62, doi: 10.1190/1.1451331.

Whitcombe, D. N., P. A. Connolly, R. L. Reagan, and T. C. Redshaw, 2002, Extended elastic impedance for fluid and lithology prediction: Geophysics, **67**, 63–67, doi: 10.1190/1.1451337.

Satinder Chopra has 33 years of experience as a geophysicist specializing in processing, reprocessing, special processing, and interactive interpretation of seismic data. He has rich experience in processing various types of data such as vertical seismic profiling, well-log data, seismic data, etc., as well as excellent communication skills, as evidenced by the many presentations and talks delivered and books, reports, and papers he has written. He has been the 2010–2011 CSEG Distinguished Lecturer, the 2011–2012 AAPG/SEG Distinguished Lecturer, and the 2014–2015 EAGE e-Distinguished Lecturer. He has published eight books and more than 400 papers and abstracts and likes to make presentations at any beckoning opportunity. His work and presentations have won several awards, the most notable ones being the EAGE Honorary Membership (2017), CSEG Honorary Membership (2014) and Meritorious Service (2005) Awards, 2014 APEGA Frank Spragins Award, the 2010 AAPG George Matson Award, and the 2013 AAPG Jules Braunstein Award, SEG Best Poster Awards (2007, 2014), CSEG Best Luncheon Talk Award (2007), and several others. His research interests focus on techniques that are aimed at the characterization of reservoirs. He is a member of SEG, CSEG, CSPG, EAGE, AAPG, and the Association of Professional Engineers and Geoscientists of Alberta (APEGA).

Ritesh Kumar Sharma received a master's (2007) degree in applied geophysics from the Indian Institute of Technology, Roorkee, India, and an M.S. (2011) in geophysics from the University of Calgary. He works as an advanced reservoir geoscientist at Arcis Seismic Solutions, TGS, Calgary. He is involved in deterministic inversions of poststack, prestack, and multicomponent data, in addition to amplitude variation with offset analysis, thin-bed reflectivity inversion, and rock-physics studies. Before joining the company in 2011, he served as a geophysicist at Hindustan Zinc Limited, Udaipur, India. He has won the best poster award for his presentation titled "*Determination of elastic constants using extended elastic impedance*" at the 2012 GeoConvention held at Calgary. He also received the Jules Braunstein Memorial Award for the best AAPG poster presentation titled "*New attribute for determination of lithology and brittleness,*" at the 2013 AAPG Annual Convention and Exhibition held in Pittsburgh. He has received the CSEG Honorable Mention for the Best Recorder Paper award in 2013. He is an active member of SEG and CSEG.

Graziella Kirtland Grech received a doctorate in exploration geophysics from the University of Calgary, Canada. She has more than 20 years of industry experience in technical and leadership roles. Since 2012, she has been the director for processing and reservoir services at Arcis (a TGS company).

Bent Erlend Kjølhamar received a master's degree in geology from the University of Oslo, and he has been working for TGS for the past 20 years. He is the TGS director of project development for Europe and Russia.